Eclética Química Journal

Original Article

revista.iq.unesp.br

| Vol. 47 | n. 3 | 2022 |

Experimental, DFT study, and *in silico* molecular docking investigations of dichlorodiphenyltrichloroethane against human estrogen receptor alpha

Tabe Ntui Ntui[1], Vincent Ndem Osabor[2], Peter Amba Neji[1], Michael Akomaye Akpe[2], John Akwagiobe Agwupuye[2+], Stephen Adie Adalikwu[3], Terkumbur Emmanuel Gber[2], Bitrus Hyelavalada Andrew[2], Uduak Ugbaja[2]

1. Cross River University of Technology, Faculty of Physical Sciences, Calabar, Nigeria.
2. University of Calabar-Nigeria, Department of Pure and Applied Chemistry, Calabar, Nigeria.
3. Cross River State College of Education, Akamkpa.

+Corresponding author: John Akwagiobe Agwupuye, **Phone**: +2348100056340, **Email address:** agwupuye.john@yahoo.com

ARTICLE INFO

Article history:
Received: November 09, 2021
Accepted: May 07, 2022
Published: July 01, 2022

Section Editor: Assis Vicente Benedetti

Keywords
1. DFT
2. molecular docking
3. DDT
4. estrogen receptor

ABSTRACT: Advanced computational tools allowed to study a pure commercial sample of dichlorodiphenyltrichloroethane (DDT) prepared in liquid phase in KBr pellets and characterized using FT-IR and GC-MS followed by the application of DDT for molecular docking against human estrogen receptor alpha. The compound was modelled using GaussView software. Using Veda 04 program, the theoretical vibrational energy distributions and experimental vibrational frequencies were compared. Interestingly, C1 and C2 possess the highest atomic charge density distribution (ACDD) of -0.284e and -0.283e while C21 and C11 have lowest ACDD of -0.064e and -0.063e in a relative manner, since the deactivating power of chlorine atoms decreases charge densities of the bonded carbon. The highest intramolecular interacting perturbation energy is 1121.92 kJ mol^{-1} occurs between π*C19–C21 donor orbital and π*C14–C16 acceptor orbital while the least intramolecular interaction occurs in the lone pair of LPC26 and the sigma nonbonding (σC1–Cl24) NBO orbitals with $E^{(2)}$ of 32.21 kJ mol^{-1}. Steric interaction was the only interaction found within the complex after the docking.

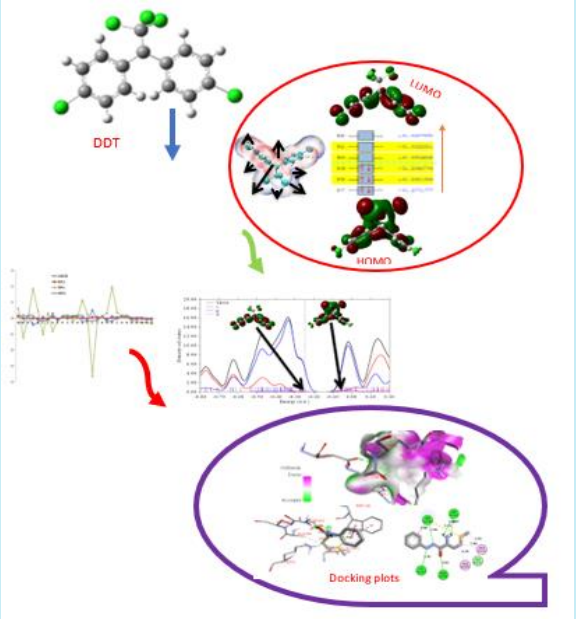

Eclética Química Journal, vol. 47, n. 3, 2022, 39-52
ISSN: 1678-4618
DOI: 10.26850/1678-4618eqj.v47.3.2022.p39-52

1. Introduction

Experimental and density functional theory (DFT) studies of the powerful insecticide dichlorodiphenyltrichloroethane (DDT), often referred to as 4^1, 4^1 – DDT have been carried out by several researchers, and studies showed that it has great impact on human health and environment in general. The DDT is one of the organochlorine pesticides (OCPs) with the potential to contaminate or pollute water and other environmental matrices due to its toxic effect on human and aquatic organisms (Buah-Kwofie *et al.*, 2018; Miao *et al.*, 2020). Notwithstanding, the persistent nature of DDT in water is due to its feeble solubility and excess half-life and the flimsy soluble nature of DDT in water results in their deposition on soil, which may either spread to the surface water or affect the groundwater. Besides, when aquatic invertebrates are subjected to DDT, it has the potential to disturb the function of the endocrine system of fishes and birds that consume them (Kowenje *et al.*, 2013; Sruthi *et al.*, 2017).

R. Zhang *et al.* (2021) studied the detoxifying mechanism of 1-chloro-4-[2, 2, 2-trichloro-1-(4-chlorophenyl) ethyl] benzene metabolized by human P450 enzymes using a combination of molecular dynamic, quantum mechanics/molecular mechanics and DFT. Their fact-findings reveals that DDT can be broken-down by P450 enzymes through the hydrogen abstraction and electrophilic addition mechanism, and the primary derivatives are epoxides (2, 3-oxide-DDT and 3, 4-oxide-DDT), DDE and dicofol. Similarly, Iramain *et al.* (2020) carried out a combine experimental (Fourier Transform Infrared (FT-IR) and Fourier Transform Raman (FT-Raman) and different DFT methodologies (B3LYP/6-31G+(d) and B3LYP/6-311++G(d, p)) studies to structurally characterized the potent insecticide dichlorodiphenyltrichloroethane (4′, 4′-DDT). Furthermore, DFT technique at the Becke-86 exchange functional and LeeYang–Parr correlation functional under generalized gradient approximation methods was used in inspecting the chemiresistive detecting potential of a buckled configuration of antimonene nanotube (SbNT) towards the water pollutants–DDT and toxaphene (Bhuvaneswari *et al.*, 2020).

The DFT calculations were carried out using B3LYP/6-31G (d) basic sets. The experimental and theoretical results for the vibrational frequency analysis were reported. The energies of the frontier molecular orbitals (FMOs) involving the highest occupied molecular orbital (HOMO) and the lowest unoccupied molecular orbital (LUMO) were analyzed with tabular and graphical representation. Fukui functions, chemical reactivity descriptors, natural bond orbital (NBO), electrostatic potential, and a comparison between three population analysis; MPA, NPA and atomic dipole moment corrected Hirshfeld (ADCH) were calculated and reported to reveal the most reactive sites in the compound and its overall reactivity.

2. Methodology

2.1 Experimental method

A pure commercial sample of liquid DDT was prepared in potassium bromide (KBr) pellets and used to study experimental FT-IR spectrum using KBr disc at wavenumber region 4000-650 cm^{-1} with a CARY 630 FTIR–Agilent technology spectrophotometer and with a spectral resolution at 8 cm^{-1}. Similarly, electrospray ionization mass spectroscopy (ESI-MS) was employed for further structural determination of DDT.

2.2 Computational method

The initial structure of l,l,l,2-tetrachloro-2,2-bis(p-chlorophenyl)ethane (DDT) was modeled using GaussView software (Fig. 1) according to the single X-ray crystal structure obtained by Hovmöller *et al.* (1978). Geometry optimization of DDT were performed using B3LYP which includes Becke's (B3) parameter exchange functional along with Lee–Yang Parr's (LYP) gradient corrected correlation functional (Lee *et al.*, 1988) using Gaussian 09 and GaussView 6.0.16 softwares (Dennington *et al.*, 2016; Frisch *et al.*, 2009). Pregeometry optimization using the molecular mechanic optimization with molecular mechanics in combination with forcefield implemented in the HyperChem program (HyperChem, 2001) has been performed on model structures and outputs used for further geometry optimization at the B3LYP/6-31+G(d,p) level of theory. Natural bond orbital analyses were calculated by the NBO 3.1 module embedded in Gaussian. In the calculation, a 6-31+G(d,p) basis set was used for the investigation, using water solvation model as an implicit approach. The QTAIM investigations and all other wavefunction analyses were conducted by Multiwfn 3.7 dev, which is a multifunctional wavefunction analysis program developed by Lu and Chen (2012). Unless otherwise specified, the default settings were used throughout these calculations. All molecular electrostatic isosurface maps were rendered by visual molecular dynamic (VMD) 1.9.3 program (Humphrey *et al.*, 1996) based on the outputs of Multiwfn analyzer.

Eclética Química Journal, vol. 47, n. 3, 2022, 39-52
ISSN: 1678-4618
DOI: 10.26850/1678-4618eqj.v47.3.2022.p39-52

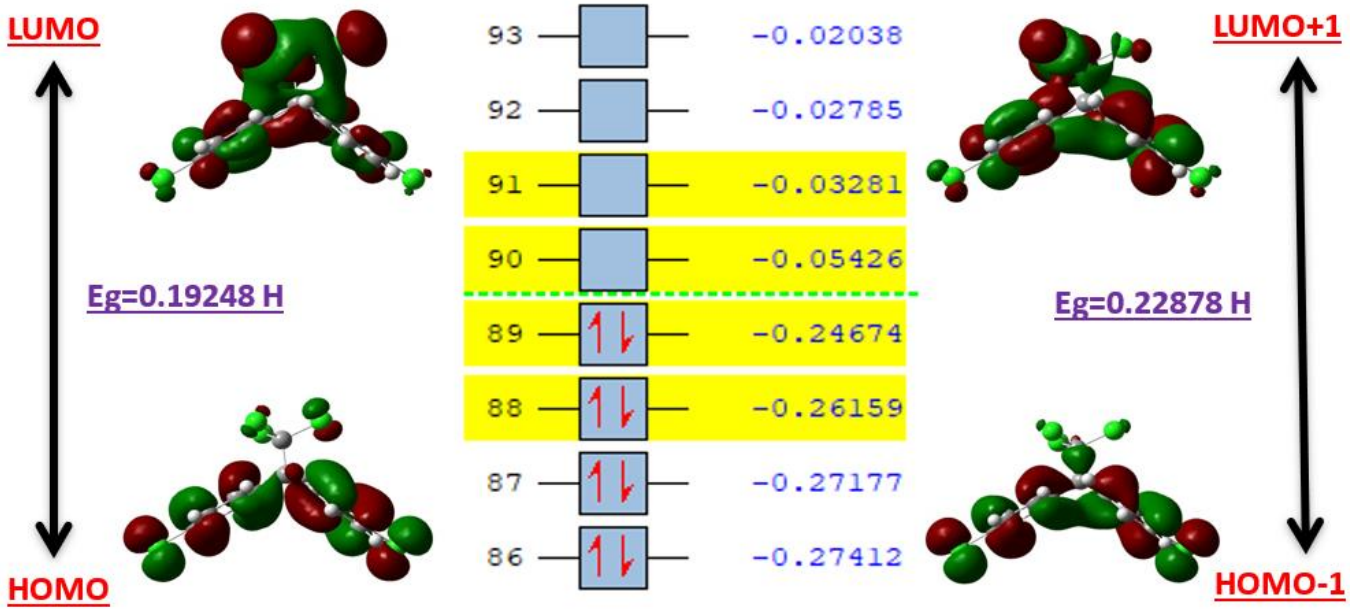

Figure 1. HOMO-LUMO of the tile molecule.
Source: Elaborated by the authors, obtained using Visual molecular dynamic (VMD) 1.9.3 program based on the outputs of Multiwfn analyzer.

3. Results and discussion

3.1 Structural analysis

3.1.1 Fourier transform infrared vibrational analysis

The vibrational modes associated with relevant and specific molecular structures of the calculated compound in question have been the main goal of the vibrational analysis. From the vibrational analysis carried out, the maximum number of possibly active noticeable fundamentals of a nonlinear molecule that contains N atoms is equal to (3N-6) usual modes of vibration (Agwupuye *et al.*, 2021a). The studied compound has 36 atoms and 102 modes of vibrations. Out of the 102 modes of vibration, 35 are stretching modes, 34 are bending modes, and 33 are torsional. The DFT computed vibration wavenumber are often of much magnitude as compared to the experimentally determined wave number owing to the DFT basic set deficiencies and the combination of electron correlation effects. Hence, factors called scale factors are used to fit the DFT computed wave numbers compared to the observed ones for accurate results fitting. The scale factor used is less than one (0.96) to reduce the overall deviation. The fundamental modes in terms of vibrational assignments associated with theoretical IR and potential energy distributions computed with the DFTB3LYP/6-311++G(d,p) method along with investigational FT-IR spectrum presented in Tab. S1 and Fig. S1 of the supporting information respectively. Few bands with weak intensity were not present in the spectra which can be confirmed by theoretically computed FT-IR intensity values.

***C*–*Cl* vibrations**: The characteristic R-NH_2 vibrations for primary amines have been assigned in the region 3500–3200 cm^{-1} (Pretsch *et al.*, 2013). Bend in primary amines results in a broadband in the range 1640–1560 cm^{-1} (Pretsch *et al.*, 2013). The present calculations place the R-NH_2 stretching modes at 3451 and 3358 cm^{-1} in experimental FT-IR. The H–N–H band was also observed experimentally to occur at 1640 cm^{-1}. The bands at 3516 and 3417 cm^{-1} for R-NH_2 stretch and 1628 cm^{-1} for N-H bond B3LYP/6-31++G(d,p) set are in good agreement with observed spectral data. These are intense stretching modes and identified from the PED in Tab. 1.

Eclética Química Journal, vol. 47, n. 2, 2022, 39-52
ISSN: 1678-4618
DOI: 10.26850/1678-4618eqj.v47.3.2022.p39-52

Table 1. Detailed assignments of fundamental experimental and theoretical vibrations of AATCo by normal mode analysis.

		Theoretical Value			
Mode No.	**Experimental IR (cm^{-1})**	**Unscaled Frequency**	**Scaled Frequency**	I_{IR}^{b}	**Assignments with $PEDd$(%)**
1	3239	3235	3106	2.10	νCH(98)
2	800	869	801	100.22	ν ClC(42)+ ν ClC(49)
6		3229	3100	4.10	νCH(84)
7		3220	3091	6.28	νCH(95)
8		3216	3087	27.29	νCH(84)
9		3206	3078	37.66	ν_{asy}CH(88)
10		3193	3065	14.70	νCH(89)
11		3183	3056	23.77	νCH(88)
12		3183	3056	5.87	νCH(88)
13		3180	3053	17.90	νCH(97)
14	2214	2316	2223	124.98	ν_{asy}(90)+νCC(10)
18		1655	1589	2.85	νCC(51)+βHCC(20)
19		1636	1571	1.61	νCC(53)+βHCC(13)
20	1607	1620	1555	16.61	νCC(53)+βHCC(10)
21		1574	1511	35.87	νCC(14)+ν_{asy} CC(12)+β'HCC(29)
22		1559	1497	283.54	ν_{asy}CC(38)+β'HCC(29)
23		1533	1472	15.54	βHCC(52)+βCCC(11)
31		1366	1311	1311	ν_{asy}(52)+βHCC(18)
32		1349	1295	3.83	βHCC(56)
33		1340	1286	6.88	νCC(39)+βHCC(25)
37		1226	1177	49.48	ν_{asy}CC(20)+βHCC(71)
38		1190	1142	0.79	βHCC(79)
39		1186	1139	0.35	β'HCC(84)
45		1049	1007	3.47	νCC(46)+βHCC(24)+βCCC(17)
46		1032	991	0.15	βHCC(11)+βCCC(70)
47		1015	974	0.13	νCC(27)+βCCC(57)
49		979	940	0.06	τHCCC(81)
53		940	902	3.85	τHCCC(83)
64		703	675	25.25	τHCCC(27)+τHCCC(13)+τRCCCC(40)
65		694	666	2.87	δCCCC(25)+τRCCCC(25)+τRCCCC(13)+δCCC(15)
66	690	654	628	1.41	βCCC(63)+βCCC(12)
67		630	605	0.12	βCCC(84)
73		534	513	21.23	βCCC(28)
81		421	404	1.41	τHCCC(13)+τRCCCC(67)
82		419	402	6.33	τRCCCC(69)
89		274	263	7.34	νCC(19)+βCCC(16)
96		115	110	0.83	δCCCC(18)
97		83	80	2.98	βCCC(10)+βCCS(10)+βCCC(14)+τCCCC(10)
98		64	61	4.58	τRCCCC(63)
99		61	59	3.30	τRCCCC(55)+δCCCC(65)

v = symmetrical stretching; v_{asy} = asymmetrical stretching; β = in plane bending; δ = out of plane bending; τ = torsional; τR = torsional ring.

Source: Elaborated by the authors using data obtained from a CARY 630 FTIR–Agilent technology spectrophotometer and Gaussian 09/ GaussView 6.0 software.

Eclética Química Journal, vol. 47, n. 3, 2022, 39-52
ISSN: 1678-4618
DOI: 10.26850/1678-4618eqj.v47.3.2022.p39-52

=$\boldsymbol{C}$−$\boldsymbol{H}$ vibrations: The C–H stretching vibration modes in the aromatic ring was observed at range 3300–3000 cm^{-1} region (Bassey *et al.*, 2022). The title compound observes =C–H stretching vibrational mode at 3239 cm^{-1} for experimental FT-IR while the computational frequency of the title compound was observed at 3106 cm^{-1}. These are intense stretching modes and identified from the PED.

$\boldsymbol{C}$−$\boldsymbol{C}$ and $\boldsymbol{C}$=$\boldsymbol{C}$ vibrations: The aromatic C=C and C−C stretching vibrations (aromatic ring stretching vibrations) arises in the region 1625–1400 cm^{-1} (Tadesse, 2017). In the present study, the observed C=C stretching vibrational modes of the title compound are 1607 and 1506 cm^{-1} in experimental FT-IR and also C–C stretching vibrational modes are assigned at 1297 and 1181 cm^{-1} respectively in experimental FTIR. The C–C–C the range 999–665 cm^{-1} was reported for planar vibration wave number by Saminathan *et al.* (2021). The experimental aromatic ring C–C–C bending vibrations of the title compound has appeared at 731 and 690 cm^{-1} in experimental FT-IR. The computationally calculated FT-IR for C=C stretching vibrations, C–C stretching vibrations, and aromatic ring C–C–C bending vibrations are 1602 and 1411, 1286 and 1190, 763 and 688 cm^{-1} respectively.

3.1.2 Electron spray ionization-mass spectrometry analysis

The ESI-MS is a high-speed and accurate spectroscopic technique used in the qualitative and quantitative identification of small organic molecules and the determination of their component molecular weights. The ESI-mass spectrum of DDT is presented in Fig. S1 of the supporting information, the peaks with higher intensity at m/z are 42.0, 125.0, 81.0, 152.0 and 170.0 and they correspond to the species C_2H_4N, $C_5H_5N_2S$, C_4HS, $C_7H_8N_2S$ and $C_{11}H_{10}N_2$. The peaks with low intensity at m/z are 53.0, 68.0, 97.0, 108.0 and 137.0. Their corresponding species are–$[C_2S]^+$, C_5H_8, C_5H_5S, N_2C_4S and $C_6H_5N_2S$.

3.2 Frontier Molecular Orbital (FMO)

The can be linked on two important parameters in quantum chemistry—HOMO and LUMO. These parameters are very important in the analysis of the reactivity and the kinetic stability of a molecule (Agwupuye *et al.*, 2021b). Within the molecule, the electron donating capability can be seeing in the HOMO, while the ability of an atom or molecule to accept electrons is indicated by the LUMO. The difference between these two parameters, which are HOMO and LUMO energies ($E_{HOMO} - E_{LUMO}$) match to the energy gap of the molecule. The bond gap depicts information which indicate the structure's stability and intramolecular interaction as a result of charge transfer from the donor and acceptor atom (Khalid *et al.*, 2020). Using Gauss View 6.0.16 software, the values of the E_{HOMO}, E_{LUMO} and energy gap were obtained maximizing the used with the output log file gotten from the free optimized structure. The computed FMO and global reactivity descriptors are reported in Tab. 2. Using the Multiwfn analyzer for calculating the HOMO-LUMO orbital compositions, the results revealed that the HOMO orbitals are majorly distributed within C_4, C_{11}, C_{14}, and C_{21} ring atoms with compositions of 13.10, 10.84, 12.75, and 11.43% respectively. However, the LUMO molecular orbital compositions are primarily situated on C_1, Cl_{25}, Cl_{24}, and Cl_{26} atoms respectively. The HOMO-LUMO molecular orbital distributions are reported in Fig. 1.

Table 2. HOMO-LUMO energy.

S/No	B3LYP/6-31+G(d)	Values
1	E_{total}	–2839.87 a.u.
2	Dipole moment	1.04 Debye
3	E_{HOMO}	–6.71 eV
4	E_{LUMO}	–1.48 eV
5	E_{gap}	5.23 eV
6	E_{HOMO-1}	–7.12 eV
7	E_{LUMO+1}	–0.89 eV
8	$E_{(HOMO-1)} - E_{(LUMO+1)}$	6.23 eV
9	μ	4.09
10	η	2.62
11	ω	3.20
12	S	0.19
13	χ	–4.09

Source: Elaborated by the authors, calculated using B3LP/6-31G(d) in Gaussian 09 software.

3.3 Natural Bond Orbital Analysis

The NBO provides a profitable technique in understanding the computational solutions of the Schrödinger equation, it also provided the convenient basis for studying the charge transfer or conjugate interaction in the molecules especially the nature of hydrogen bonding and also interaction among bonds (Agwupuye *et al.*, 2021b). This parameter is very significant in studying the interactions of donor and acceptor orbitals of molecules that enables the understanding of intra- and intermolecular bonding and

Eclética Química Journal, vol. 47, n. 2, 2022, 39-52
ISSN: 1678-4618
DOI: 10.26850/1678-4618eqj.v47.3.2022.p39-52

interactions. Donor occupied orbitals can interact strongly (Suresh *et al.*, 2014). Second-order perturbation Fock matrix was carried out to study the Lewis valence orbital (donor) i, non-Lewis valence orbital (acceptor) j, interactions in the NBO basis. The stabilization energy associated with the electron delocalization between Lewis (filled) and non-Lewis (unfilled) is estimated in Eq. 1 (Armaković *et al.*, 2012; Enudi *et al.*, 2021).

$$E^{(2)} = \Delta E_{i,j} = q_i \frac{F^2(i,j)}{\varepsilon_i - \varepsilon_j} \quad (1)$$

From the equation above, the donor orbital occupancy was represented by q_i the donor orbital occupancy, ε_i and ε_j represent the diagonal elements, and the Fock matrix elements were represented by $F_{(i,j)}$. The larger perturbation energy value also called the stabilization energy value $E^{(2)}$ depicts a stronger interaction between electron donors and electron acceptors, i.e., the greater extent of conjugation of the whole system and the more donating tendency from the electron donors to electron acceptor was vividly understood by this analysis. NBO analysis of the studied structure has been performed by using the DFT/B3LYP/6- 311+G(d) level of theory (Agwupuye *et al.*, 2021c) to understand clearly the charge transfer or conjugative interaction, delocalization of electron density in the molecule and energy of interaction as reported in Tab. 3. From the results, the highest intramolecular interacting perturbation energy is 1122 kJ mol^{-1} occurring between $\pi^*C_{19} - C_{21}$ donor orbital and $\pi^*C_{14} - C_{16}$ acceptor orbital while the least intramolecular interaction is observed to occur in the lone pair of πpC_{26} and the sigma nonbonding ($\sigma C_1 - Cl_{24}$) NBO orbitals having $E^{(2)}$ energy of 32 kJ mol^{-1}.

Table 3. NBO second order perturbation energies for the studied compound.

S/NO	Donor	Acceptor	$E^{(2)}$(kcal mol^{-1})	$E(i) - E(j)$	$F(i,j)$
1	$\pi^*C_{19} - C_{21}$	$\pi^*C_{14} - C_{16}$	268.21	0.01	0.094
2	$\pi^*C_9 - C_{11}$	$\pi^*C_4 - C_6$	255.27	0.01	0.084
3	$\pi^*C_{19} - C_{21}$	$\pi^*C_{15} - C_{17}$	218.48	0.01	0.800
4	$\pi^*C_9 - C_{11}$	$\pi^*C_5 - C_7$	184.74	0.01	0.079
5	$\pi^*C_{14} - C_{16}$	$\pi^*C_{19} - C_{21}$	21.57	0.27	0.069
6	$\pi^*C_{15} - C_{17}$	$\pi^*C_{19} - C_{21}$	20.49	0.27	0.067
7	$\pi^*C_{19} - C_{21}$	$\pi^*C_{15} - C_{17}$	19.58	0.30	0.068
8	$\pi^*C_{19} - C_{21}$	$\pi^*C_{14} - C_{16}$	18.99	0.30	0.067
9	πpCl_{28}	$\pi^*C_9 - C_{11}$	12.28	0.33	0.062
10	πpC_{26}	$\sigma C_1 - Cl_{24}$	7.70	0.39	0.043

Source: Elaborated by the authors, calculated using NBO 3.1 module embedded in Gaussian 09 software.

3.4 Population Analysis

DFT study of atomic charge is very important analysis in describing the distribution and location of ionic charges within the molecule thereby predicting the individual atomic reactivity. This is very relevant in many areas of studies as it stretches across the field of quantum chemistry and molecular modeling, details of electrostatic interaction with molecular force fields can also be provided by this analysis (Agwupuye *et al.*, 2021a) Using Mulliken Population Analysis (MPA), the atomic charges of the studied DDT in this present study are obtained, Hirshfeld (HPA), Atomic dipole moment corrected Hirshfeld (ADCH), and Becke (BPA) methods. The computational population result for the charge distributions for the different methods is presented in Fig. 2. It is observed that C_1 and C_2 possess the highest atomic charge density distribution of -0.284 and -0.283e while C_{21} and C_{11} are less with atomic charge distribution of -0.064 and -0.063e respectively. This is caused by the electron withdrawing power of the chlorine atoms resulting in decreasing in charge densities of the bonded carbon.

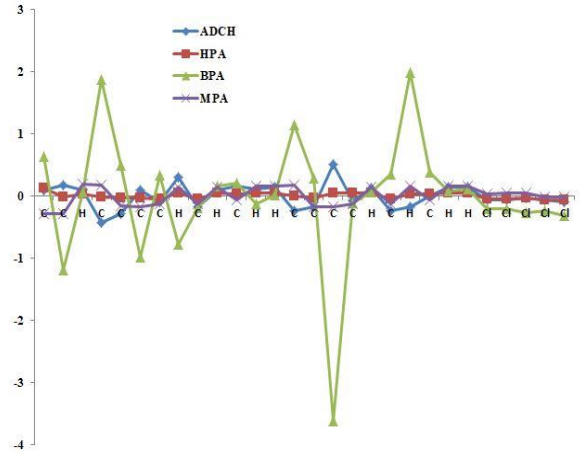

Figure 2. Population analysis plot.
Source: Elaborated by the authors, plotted using multiwfn analyzer software.

Eclética Química Journal, vol. 47, n. 3, 2022, 39-52
ISSN: 1678-4618
DOI: 10.26850/1678-4618eqj.v47.3.2022.p39-52

3.5 Absorption Study

The excitation type, energy, wavelength, oscillator strength, and major orbital contributions in both gas and solvents are presented in Tabs. 4 and 5 respectively. The studied compound has vertical excitation energies of 5.34 and 5.37 eV with associated wavelengths of 232 and 230 nm in gas and solvents respectively. In the gas phase, the prominent intense absorption (of 21.39% orbital contributions) arises as a result of electronic transitions from HOMO (89) → LUMO+2 (91) molecular orbital. It can also be deduced that the electron density is uniformly distributed throughout within the LUMO in the molecule, as the result of the electron withdrawing moiety it is shifted towards the LUMO and LUMO+2 transition accordingly.

Table 4. Excitation energies and oscillator strength in solvation.

Excitation type	E/eV	λ(nm)	f	Major contributions	Assignment
$S_O \rightarrow S_1$	5.3436	232.02	0.0104	89 →91 (21.39%) 86 →92 (11.49%) 89 →92 (10.05%)	π → π*
$S_0 \rightarrow S_2$	5.3601	231.31	0.0107	89 →93 (20.00%) 89 →90 (17.02%) 89 →92 (10.88%)	π → π*
$S_0 \rightarrow S_3$	5.6127	220.90	0.3030	89 →90 (71.58%) 89 →93 (5.40%) 88 →92 (3.15%)	π → π*
$S_0 \rightarrow S_4$	6.0123	206.22	0.1097	88 →90 (45.09%) 89 →94 (11.36%) 89 →92 (11.03%)	π → π*
$S_0 \rightarrow S_5$	6.1582	201.33	0.0537	89 →91 (26.72%) 85 →90 (14.31%) 89 →92 (10.08%)	π → π*

Source: Elaborated by the authors, calculated using DFT/B3LYP/6- 311+G(d).

In the solvents, a similar transition is involved between HOMO → LUMO+2 molecular orbitals with an oscillator strength of 0.0207. Other LUMO orbitals having different vertical excitations in solvents are LUMO+3 and LUMO+5 having orbital contributions of 12.66 and 12.93% respectively. For all the ground state (S_0) to the fifth singlet states (S_1), $S_0 \rightarrow S_1$ first vertical singlet states transition has the highest orbital contributions in solvents involving HOMO-2 to LUMO orbitals.

Table 5. Excitation energies and oscillator strength in solvation.

Excitation type	E/eV	λ(nm)	f	Major contributions	Assignment
$S_0 \rightarrow S_1$	5.3730	230.75	0.0207	89 →91 (13.18%) 89 →92 (12.66%) 89 →94 (12.93%)	π → π*
$S_0 \rightarrow S_2$	5.3794	230.48	0.0150	87 →90 (100.46%) 89 →93 (16.56%) 88 →92 (9.31%)	π → π*
$S_0 \rightarrow S_3$	5.5677	222.69	0.3205	89 →90 (70.20%) 88 →92 (4.00%) 89 →94 (3.71%)	π → π*
$S_0 \rightarrow S_4$	5.9995	206.66	0.1320	88 →90 (47.5859) 89 →92 (10.30%) 88 →91 (6.76%)	π → π*
$S_0 \rightarrow S_5$	6.1053	203.07	0.1008	89 →92 (44.37%) 89 →90 (10.82%) 89 →92 (5.35%)	π → π*

Source: Elaborated by the authors, calculated using multiwfn software.

Eclética Química Journal, vol. 47, n. 3, 2022, 39-52
ISSN: 1678-4618
DOI: 10.26850/1678-4618eqj.v47.3.2022.p39-52

3.6 Molecular Electrostatic Potential

Molecular electrostatic potential diagrams are primarily used to show the electron density distribution difference in a compound. In the title molecule, electron density is evident around the DDT ring without any significant distortion. The distance of these electrons apart is also indicated as can be seen in Fig. 3.

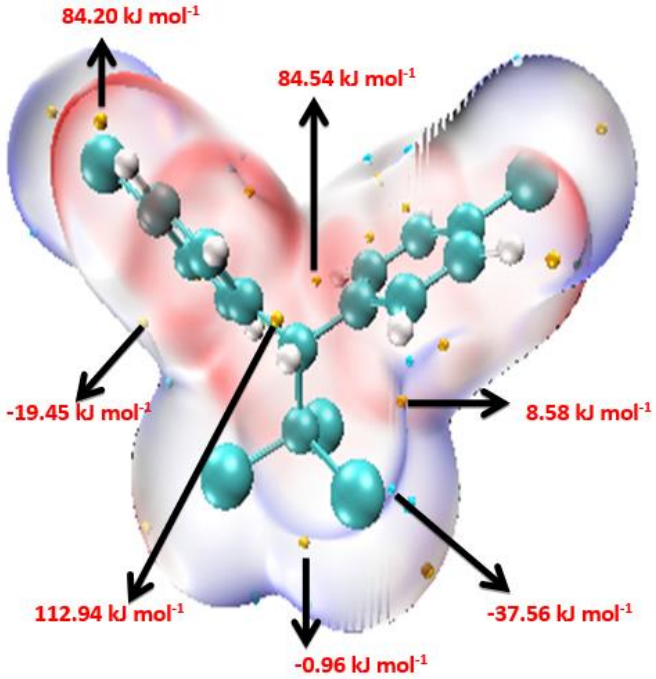

Figure 3. Molecular electrostatic potential map of the title molecule.
Source: Elaborated by the authors. Isosurface maps were rendered by visual molecular dynamic (VMD) 1.9.3 program based on the outputs of Multiwfn analyzer.

3.7 Density of States

Density-of-state (DOS) is essentially the number of different states at a particular energy level that electrons are allowed to occupy, and it is very vital in this kind of study to appropriately characterized orbital composition by visualizing them. In the underlying curves, the plots show the different energy levels in unit energy interval at the number of molecular orbitals. Multiwfn analyzer was used in plotting the total DOS (TDOS) map for the title molecule with contribution from different sets of molecular orbitals (Fig. 4) (Liu *et al.*, 2020) and the prominent curves are denoted by the colored peaks.

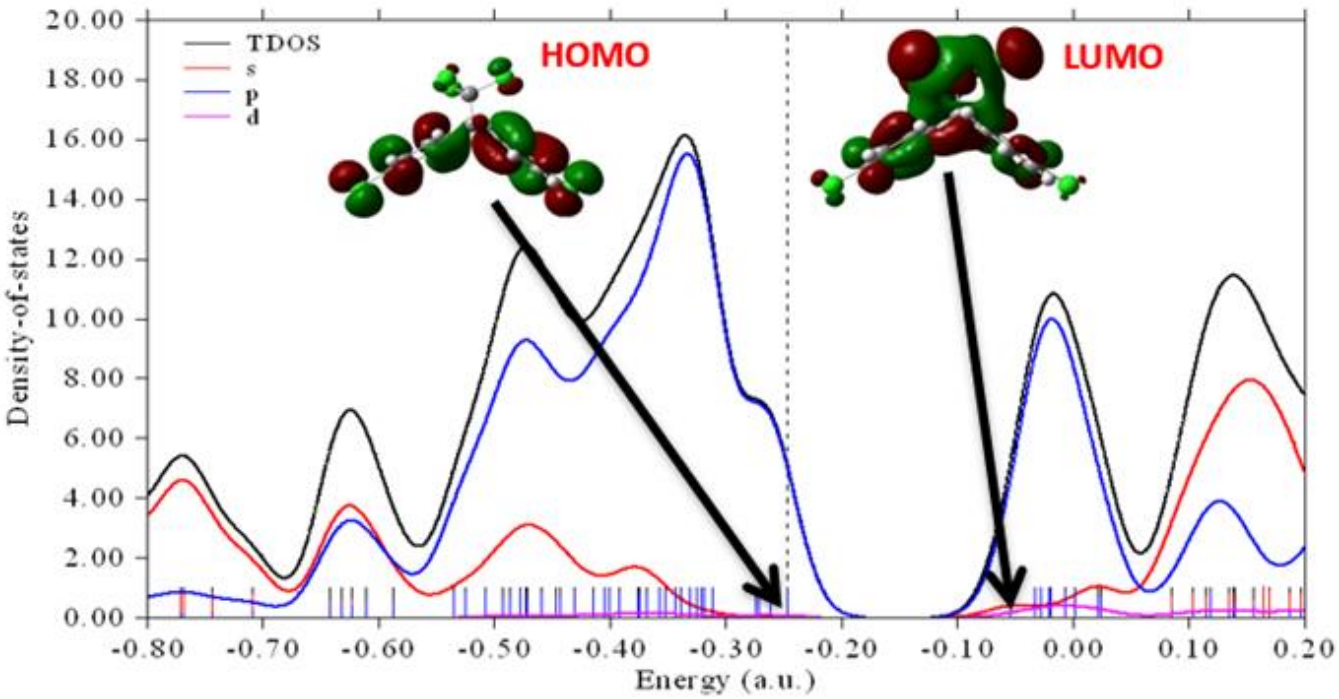

Figure 4. Density of states plot for DDT.
Source: Elaborated by the authors, plotted using Multiwfn analyzer software.

Eclética Química Journal, vol. 47, n. 3, 2022, 39-52
ISSN: 1678-4618
DOI: 10.26850/1678-4618eqj.v47.3.2022.p39-52

3.8 Nonlinear optics

Nonlinear response of properties like amplitude, phase, frequency and other propagation features of incident fields were clearly explained by nonlinear optics. The interaction of applied electromagnetic radiation to produce new fields form incidents one coins the term nonlinear optical effects (Ray, 2010). The growth of nonlinear optical materials has attracted important attention in fundamental and applied research. Nonlinear optical materials have vast applications in technologies such as in the design of information storage, processing of signal, switching of optical and design of optoelectronic devices in modern communication technology (Y. Zhang and Wang, 2017). Highly delocalized π − electron parts in a molecule and also high electron donors and acceptors containing organic materials are very good sources of nonlinear optical materials (Prasad and Ulrich, 2012). Taylor's series expansion of the total dipole moment, μtot induced by the field is used to present the NLO response of an isolated molecule in an electric field (ω) Eq. 2.

$$\mu_i(E_i) = \mu_i + a_{ij}E_j + \frac{1}{2!}\beta_{ijk}E_jE_k + \frac{1}{3!}\gamma_{ijkl}E_jE_kE_l + \cdots \quad (2)$$

where, E_i is the homogenous electric field, $\mu_i(E)$ is known as the dipole moment in an electric field, μ_i is refers to dipole moments at zero field, α_{ij}, β_{ijk}, γ_{ijkl} are the polarizability tensor component, first-order hyperpolarizability component, and second-order hyperpolarizability component respectively. Using the x, y, and z components, electric dipole moment (μ) (Eq. 3) and the average polarizability (α_{tot}) (Eq. 4) can be obtained as:

$$\mu = \sqrt{(\mu_x^2 + \mu_y^2 + \mu_z^2} \quad (3)$$

$$\alpha_{tot} = \frac{\alpha_{xx}+\alpha_{yy}+\alpha_{zz}}{3} \quad (4)$$

Anisotropy of polarizability, Eq. 5.

$$\Delta\alpha = 2^{-1}/_2\left[(\alpha_{xx} - \alpha_{yy})^2 + (\alpha_{yy} - \alpha_{zz})^2 + (\alpha_{zz} - \alpha_{xx})^2\right]^{1/_2} \quad (5)$$

The first order polarizability (β_{ijk}) is a 3rd rank tensor (3 × 3 × 3 matrix). The magnitude of the first order hyperpolarizability i is calculated using the Eq. 6.

$$\beta_{tot} = \sqrt{\beta_1^2 + \beta_2^2 + \beta_3^2} \quad (6)$$

Where, beta is given by Eq. 7:

$$\beta_i = \frac{1}{3}\sum_{j=1}^{3}(\beta_{ijj} + \beta_{jij} + \beta_{jji}) = \sum_{j=1}^{3}\beta_{ijj} \quad (7)$$

Here i, j = x, y, and z. and the final form resulting from Kleinman symmetry (Isborn et al, 2007).

The calculations were carried out by incorporating polar keyword and B3LYP functional and 6 – 311 + G(d) basis set and the output was loaded lunching multiwave function analyzer where the results obtained and presented in Tab. 6.

Table 6. The electric dipole moment (μ), polarizability ($\Delta\alpha$), and first order hyper polarizability (β) of reduced compound by B3LYP/6-311+G(d,p) approach and Multi wave function analyzer.

Parameter	Value
μ_x	0.355
μ_y	–0.204
μ_z	–0.002
μ_{Total}	0.410
Parameter	**Value**
α_{xx}	171.175
α_{xy}	11.897
α_{yy}	159.84
α_{xz}	0.811
α_{yz}	2.334
α_{zz}	255.023
α_{Total}	88.786
$\Delta\mu_{Total}$	537.319
Parameter	**Value**
β_{xxx}	–26.884
β_{xxy}	–11.862
β_{xyy}	–65.056
β_{yyy}	–165.703
β_{xxz}	2.624
β_{xyz}	17.599
β_{yyz}	52.314
β_{xzz}	–1355.432
β_{yzz}	–355.432
β_{zzz}	87.982
β_{Total}	597.706

Source: Elaborated by the authors, calculated using B3LYP/6-311+G(d,p) and Multiwfn analyzer.

3.9 Molecular docking studies

Molecular docking studies were carried out using human estrogen receptor alpha for human X-ray

Eclética Química Journal, vol. 47, n. 3, 2022, 39-52
ISSN: 1678-4618
DOI: 10.26850/1678-4618eqj.v47.3.2022.p39-52

structures (1R5K, 1ERR, 2BJ4 and 3ERT) cocrystallized with DDT. The structure of the compound was drawn using Gassian 09 (Glendening *et al.*, 2018). The optimize structure of the compound was use in Multiwfn (Lu, 2017) to invoke the different atomic number in order to know the specific atoms that interacted with the deferent amino acid. The main purpose of molecular docking is to obtain an optimized conformation for each of the drug and protein with relative orientation between them such that the free energy of the overall system is minimized (Mascarenhas and Ghoshal, 2008). It is a computational tools and techniques employed in predicting and evaluating the suitability of the studied compounds as drug candidate. It is a method that analysis the orientation and conformation of molecules into the binding site of a macromolecular targe. Toward this objective, comparative molecular docking was employed to study the drug delivery of human estrogen receptor alpha for human X-ray against DDT. The receptor proteins were prepared by removing water molecule, adding explicit hydrogens, charges and correction of deformation in amino acid sequence. The active sites of the receptor protein were predicted and defined based on the interaction of the crystallographic ligand and the complexes with the receptor molecules respectively as visualized with the discovery studio visualizer. This aims at predicting the type of interactions and the docking procedure also aims to identify and recognize the correct and most favorable binding poses within the binding site of the studied protein (Pagadala *et al.*, 2017). From these docking results hydrogen bonding was not the only bonding type that exists in the studied compounds, other interaction like unfavorable Donor–Donor bond, pi cation, pi sigma, pi alkyl, salt bridge and other as can be seen in 2D and 3D plots. However, for each receptor interaction with DDT the highest pose was recorded as –34, –26, –25 and –32 kJ mol^{-1} for 1ERR-DDT, 1R5K-DDT, 2BJ4-DDT and 3ERT respectively. These interactions are shown in Fig. 5a and 5b from this docking result, it can be seen that DDT interaction with 1ERR have the highest binding affinity compared to other receptors. The 3D structure of the hERα within the receptor backbone is presented in Fig. 5b. This steric effect that was observed in the docking result is due to the constituent atoms that make up the molecule occupy some degree of space, and when atoms come too close together there's a rise in the energy of the molecule due to the atoms being forced to occupy the same physical space. This explains why steric effect can have a dramatic effect on the observed or preferred shape of a molecule and in some cases even its chemical reactivity (Barnes, 2019; Yang *et al.*, 2010).

The docking results of the DDT 1ERR, 1R5K, 2BJ4 and 3ERT as well as the root means square distance in reference to the first mode are presented in Tab. 7.

Table 7. Binding affinities and root mean square distance of the docking score.

Receptors	Binding affinity (kJ mol^{-1})	Rmsd (I.b)	Rmsd (u.b)
1ERR	–33.9	2.448	5.061
1R5K	–25.9	2.122	3.872
2BJ4	–25.1	1.169	5.252
3ERT	–32.2	1.297	4.858

Source: Elaborated by the authors, calculated using autoDoc Vina tools.

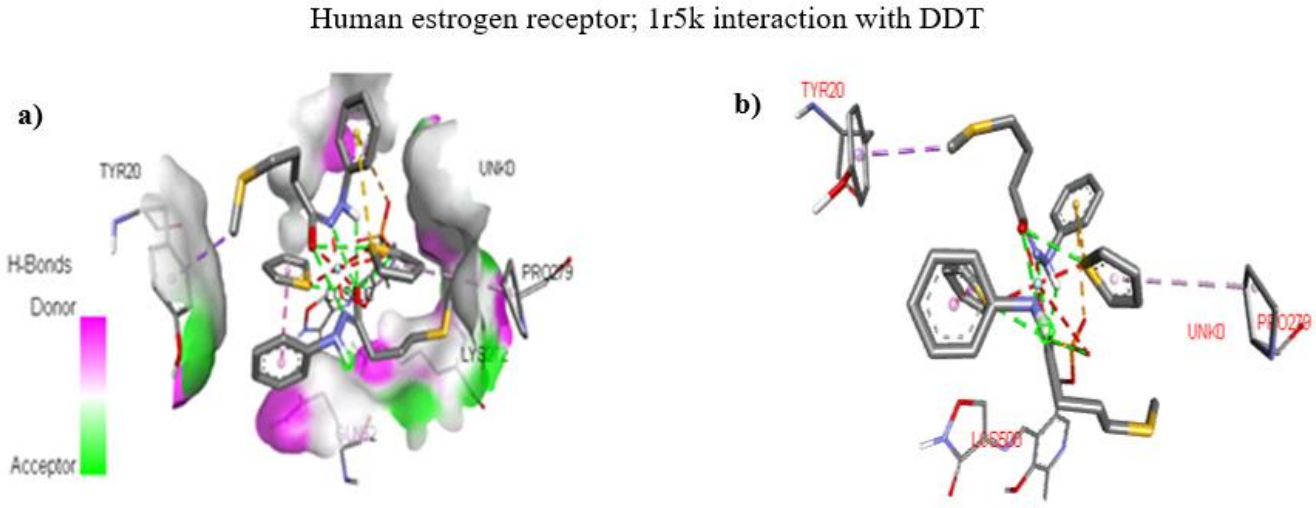

Eclética Química Journal, vol. 47, n. 3, 2022, 39-52
ISSN: 1678-4618
DOI: 10.26850/1678-4618eqj.v47.3.2022.p39-52

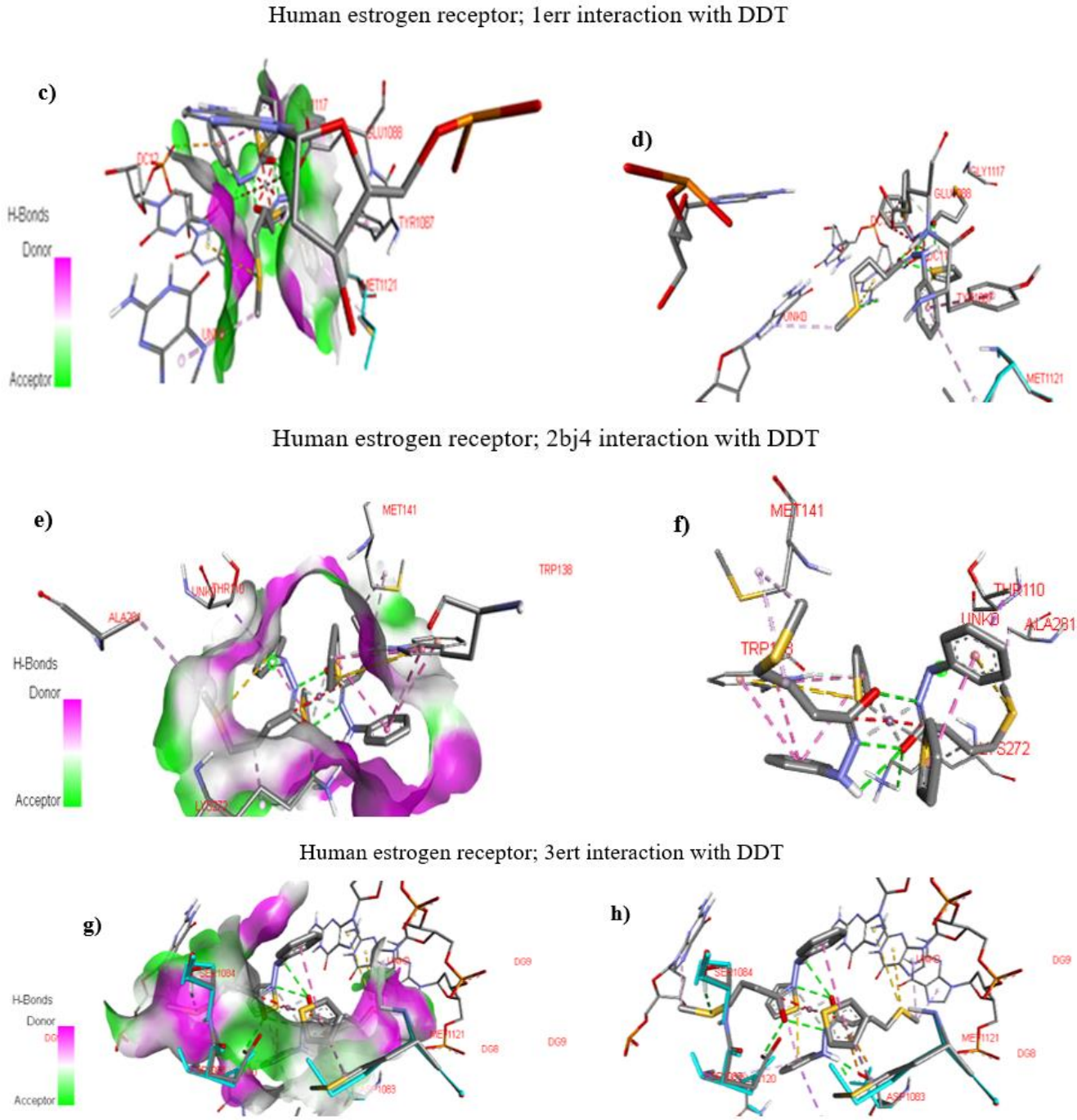

Figure 5. Showing 3D, steric interactions and other forms of interaction of the human estrogen receptor alpha X-ray structures as cocrystallized with DDT.
Source: Elaborated by the authors, Generated using AutoDoc Vina tools.

4. Conclusions

High level quantum computational tools were used to study a pure commercial sample of DDT prepared in liquid phase in KBr pellets and characterized using FT-IR and GC-MS followed by the application of the title molecule for molecular docking against human estrogen receptor alpha (hERα). Using water model as an implicit approach, the high calculations were computed using a 6 – 31 + G(d,p) basic set. The fundamental modes in terms of vibrational assignments associated with theoretical IR and potential energy distributions were computed by the use the DFT-B3LYP/6-311++G(d,p) basic sets along with experimental FT-IR spectrum. It was observed that bands with weak intensity were not existing in the

Eclética Química Journal, vol. 47, n. 3, 2022, 39-52
ISSN: 1678-4618
DOI: 10.26850/1678-4618eqj.v47.3.2022.p39-52

spectra, and this was confirmed with theoretically calculated FT-IR intensity values. Using Multiwfn analyzer for calculating the HOMO-LUMO orbital compositions, the results revealed that the HOMO orbitals are majorly distributed within C_4, C_{11}, C_{14}, and C_{21} ring atoms with compositions of 13.10, 10.84, 12.75, and 11.43% respectively. However, the LUMO molecular orbital compositions are primarily situated on C_1, Cl_{25}, Cl_{24}, and Cl_{26} atoms respectively. From the NBO result, the highest intramolecular interacting perturbation energy is 1122 kJ/mol occurring between $\pi^*C_{19} - C_{21}$ donor orbital and $\pi^*C_{14} - C_{16}$ acceptor orbital while the least intramolecular interaction is observed to occur in the lone pair of electron from πpC_{26} and the sigma nonbonding ($\sigma C_1 - Cl_{24}$) NBO orbitals having $E^{(2)}$ energy of 32 kJ/mol. ADCH analysis shows that C_1 and C_2 possess the highest atomic charge density distribution of –0.284 and –0.283e while C_{21} and C_{11} are less with atomic charge distribution of –0.064 and –0.063e accordingly. The electron withdrawing power of chlorine atoms in the molecules was observed to be the cause of this changes resulting in decreasing in charge densities of the bonded carbon. And in the adsorption studies, all the ground state (S_0) to the fifth singlet states (S_1), $S_0 \rightarrow S_1$ first vertical singlet states transition has the highest orbital contributions in solvents involving HOMO-2 to LUMO orbitals. While in the molecular docking studies, steric interaction was the only observable interaction that was found within the complex after the docking however, there were no observable hydrogen interactions between the drug (DDT) and any of the hERα, which would have been the bases for determining the drug activeness with the receptors.

Authors' contribution

Conceptualization: Tabe N. Ntui, John A. Agwupuye, Terkumbur E. Gber
Data curation: Stephen A. Adalikwu, Michael A. Akpe
Formal Analysis: John A. Agwupuye
Funding acquisition: Uduak Ugbaja, Tabe N. Ntui, Michael A. Akpe
Investigation: Bitrus H Andrew, Terkumbur E. Gber, John A. Agwupuye
Methodology: John A. Agwupuye, Tabe N. Ntui
Project administration: Vincent N. Osabor, Peter A. Neji, John A. Agwupuye
Resources: Michael A. Akpe, Stephen A. Adalikwu.
Software: Terkumbur E. Gber, John A. Agwupuye
Supervision: Tabe N. Ntui, Vincent N. Osabor, Peter A. Neji
Validation: John A. Agwupuye, Terkumbur E. Gber
Visualization: John A. Agwupuye
Writing – original draft: Terkumbur E. Gber
Writing – review & editing: John A. Agwupuye

Data availability statement

GC-MS, FT-IR analysis was carried at Central Laboratory at Usman Dan Fodio University, Sokoto – Nigeria and the DFT analysis was coducted using Gaussian 09, GaussView 6.0.16, and multiwfn 3.7 softwares.

Funding

Not applicable.

Acknowledgments

Tabe Ntui is very thankful to his Supervisor, Dr. Peter Neji and Hitler Louis for his immense support and contributions.

References

Agwupuye, J. A.; Louis, H.; Enudi, O. C.; Unimuke, T. O.; Edim, M. M. Theoretical insight into electronic and molecular properties of halogenated (F, Cl, Br) and hetero-atom (N, O, S) doped cyclooctane. *Mater. Chem. Phys.* **2021a**, *275*, 125239. https://doi.org/10.1016/j.matchemphys.2021.125239

Agwupuye, J. A.; Louis, H.; Unimuke, T. O.; David, P.; Ubana, E. I.; Moshood, Y. L. Electronic structure investigation of the stability, reactivity, NBO analysis, thermodynamics, and the nature of the interactions in methyl-substituted imidazolium-based ionic liquids. *J. Mol. Liq.* **2021b**, *337*, 116458. https://doi.org/10.1016/j.molliq.2021.116458

Agwupuye, J. A.; Neji, P. A.; Louis, H.; Odey, J. O.; Unimuke, T. O.; Bisiong, E. A.; Ntui, T. N. Investigation on electronic structure, vibrational spectra, NBO analysis, and molecular docking studies of aflatoxins and selected emerging mycotoxins against wild-type androgen receptor. *Heliyon.* **2021c**, *7* (7), e07544. https://doi.org/10.1016/j.heliyon.2021.e07544

Armaković, S.; Armaković, S. J.; Šetrajčić, J. P.; Šetrajčić, I. J. Active components of frequently used β-blockers from the

aspect of computational study. *J. Mol. Model.* **2012**, *18* (9), 4491–4501. https://doi.org/10.1007/s00894-012-1457-5

Barnes K. *What is the Steric Effect in Organic Chemistry? - Definition & Examples*. Study.com. 2019. https://study.com/academy/lesson/what-is-the-steric-effect-in-organic-chemistry-definition-examples.html#:~:text=The%20steric%20effect%20is%20when,occupy%20the%20same%20physical%20space (accessed 2022-06-26).

Bassey, V. M.; Apebende, C. G.; Idante, P. S.; Louis, H.; Emori, W.; Cheng, C. R.; Asogwa, F. C. Vibrational characterization and molecular electronic investigations of 2-acetyl-5-methylfuran using FT-IR, FT-Raman, UV–VIS, NMR, and DFT methods. *J. Fluoresc.* **2022**, *32* (3), 1005–1017. https://doi.org/10.1007/s10895-022-02903-8

Bhuvaneswari, R.; Nagarajan, V.; Chandiramouli, R. Sensing studies of DDT and Toxaphene molecules using chemi-resistive β-antimonene nanotubes based on first-principles insights. *Chem. Phys. Lett.* **2020**, *757*, 137895. https://doi.org/10.1016/j.cplett.2020.137895

Buah-Kwofie, A.; Humphries, M. S.; Pillay, L. Bioaccumulation and risk assessment of organochlorine pesticides in fish from a global biodiversity hotspot: iSimangaliso Wetland Park, South Africa. *Sci. Total Environ.* **2018**, *621*, 273–281. https://doi.org/10.1016/j.scitotenv.2017.11.212

Dennington, R.; Keith, T. A.; Millam, J. M. GaussView 6.0. 16. Semichem Inc.: Shawnee Mission, KS, USA. 2016.

Enudi, O. C.; Louis, H.; Edim, M. M.; Agwupuye, J. A.; Ekpen, F. O.; Bisong, E. A.; Utsu, P. M. Understanding the aqueous chemistry of quinoline and the diazanaphthalenes: insight from DFT study. *Heliyon.* **2021**, *7* (7), e07531. https://doi.org/10.1016/j.heliyon.2021.e07531

Frisch, M. J.; Trucks, G. W.; Schlegel, H. B.; Scuseria, G. E.; Robb, M. A.; Cheeseman, J. R.; Scalmani, G.; Barone, V.; Mennucci, B.; Petersson, G. A.; Nakatsuji, H.; Caricato, M.; Li, X.; Hratchian, H. P.; Izmaylov, A. F.; Bloino, J.; Zheng, G.; Sonnenberg, J. L.; Hada, M.; Ehara, M.; Toyota, K.; Fukuda, R.; Hasegawa, J.; Ishida, M.; Nakajima, T.; Honda, Y.; Kitao, O.; Nakai, H.; Vreven, T.; Montgomery Jr., J. A.; Peralta, J. E.; Ogliaro, F.; Bearpark, M.; Heyd, J. J.; Brothers, E.; Kudin, K. N.; Staroverov, V. N.; Kobayashi, R.; Normand, J. ; Raghavachari, K.; Rendell, A.; Burant, J. C.; Iyengar, S. S.; Tomasi, J.; Cossi, M.; Rega, N.; Millam, J. M.; Klene, M.; Knox, J. E.; Cross, J. B.; Bakken, V.; Adamo, C.; Jaramillo, J.; Gomperts, R.; Stratmann, R. E.; Yazyev, O.; Austin, A. J.; Cammi, R..; Pomelli, C.; Ochterski, J. W.; Martin, R. L.; Morokuma, K.; Zakrzewski, V. G.; Voth, G. A.; Salvador, P.; Dannenberg, J. J.; Dapprich, S.; Daniels, A. D.; Farkas, Ö.; Foresman, J. B.; Ortiz, J. V.; Cioslowski, J.; Fox, D. J. Gaussian 09 (Gaussian, Inc., Wallingford CT, 2009).

Glendening, E. D.; Badenhoop, J. K.; Reed, A. E.; Carpenter, J. E.; Bohmann, J. A.; Morales, C. M.; Karafiloglou, P.; Landis, C. R.; Weinhold, F. *NBO 7.0*, Theoretical Chemistry Institute, University of Wisconsin, Madison, 2018. https://nbo7.chem.wisc.edu/biblio_css.htm (accessed 2022-06-26).

Hovmöller, S.; Smith, G.; Kennard, C. H. L. Structural Studies of Polychlorinated Hydrocarbons. V. 1, 1, 1, 2-Tetrachloro-2, 2-bis (*p*-chlorophenyl) ethane and 1, 1, 1-Tribromo-2, 2-bis (*p*-chlorophenyl) ethane. *Acta Cryst.* **1978**, *B34* (10), 3016–3021. https://doi.org/10.1107/S0567740878009942

Humphrey, W.; Dalke, A.; Schulten, K. VMD: visual molecular dynamics. *J. Mol. Graph.* **1996**, *14* (1), 33–38. https://doi.org/10.1016/0263-7855(96)00018-5

HyperChem, T. HyperChem 8.07, HyperChem Professional Program. Gainesville, Hypercube. 2001.

Iramain, M. A.; Castillo, M. V.; Davies, L.; Manzur, M. E.; Brandan, S. A. Structural and SQMFF study of potent insecticide 4′, 4′-DDT combining the FT-IR and FT-Raman spectra with DFT calculations. *J. Mol. Struct.* **2020**, *1199*, 126964. https://doi.org/10.1016/j.molstruc.2019.126964

Isborn, C. M.; Leclercq, A.; Vila, F. D.; Dalton, J. L.; Brédas, L. R.; Eichinger, B. E.; Robinson. B. H. Comparison of static first hyperpolarizabilities calculated with various quantum mechanical methods. *J. Phys. Chem. A.* **2007**, *111* (7) 1319–1327. https://doi.org/10.1021/jp064096g

Khalid, M.; Ali, A.; Adeel, M.; Din, Z. U.; Tahir, M. N.; Rodrigues-Filho, E.; Khan, M. U. Facile preparation, characterization, SC-XRD and DFT/DTDFT study of diversely functionalized unsymmetrical bis-aryl-α, β-unsaturated ketone derivatives. *J. Mol. Struct.* **2020**, *1206*, 127755. https://doi.org/10.1016/j.molstruc.2020.127755

Kowenje, C. O.; Osewe, E. T.; Lalah, J. O. Effects of faujasite X and Y zeolites on the 1,1,1- trichloro-2, 2'bis (p-chlorophenyl) ethane (DDT) degradation during water purification. *Int. J. Environ. Pollut.* **2013**, *1* (1), 9–15. https://doi.org/10.11648/j.ijepp.20130101.12

Lee, C.; Yang, W.; Parr, R. G. Development of the colle-salveti correlation energy formula into a functional of the electron density. *Phys. Rev. B.* **1988**, *37* (2), 785–789. https://doi.org/10.1103/PhysRevB.37.785

Liu, Z.; Lu, T.; Chen, Q. An sp-hybridized all-carboatomic ring, cyclo[18]carbon: Electronic structure, electronic spectrum, and optical nonlinearity. *Carbon* **2020**, *165*, 461–467. https://doi.org/10.1016/j.carbon.2020.05.023

Lu, T.; Chen, F. Multiwfn: a multifunctional wavefunction analyzer. *J. Comput. Chem.* **2012**, *33* (5), 580–592. https://doi.org/10.1002/jcc.22885

Lu, T. *Multiwfn (a multifunctional wavefunction analyzer), software manual*. Beijing Kein Research Center for Natural Sciences; Version 3.4, 2017. https://web.mit.edu/multiwfn_v3.4/Manual_3.4.pdf (accessed 2022-06-26).

Mascarenhas, N. M.; Ghoshal, N. An efficient tool for identifying inhibitors based on 3D-QSAR and docking using feature-shape pharmacophore of biologically active conformation–A case study with CDK2/CyclinA. *Eur. J. Med. Chem.* **2008**, *43* (12), 2807–2818. https://doi.org/10.1016/j.ejmech.2007.10.016

Miao, J.; Liu, A.; Wu, L.; Yu, M.; Wei, W.; Liu, S. Magnetic ferroferric oxide and polydopamine molecularly imprinted polymer nanocomposites based electrochemical impedance sensor for the selective separation and sensitive determination of dichlorodiphenyltrichloroethane (DDT). *Anal. Chim. Acta.* **2020**, *1095*, 82–92. https://doi.org/10.1016/j.aca.2019.10.027

Pagadala, N. S.; Syed, K.; Tuszynski, J. Software for molecular docking: a review. *Biophys. Rev.* **2017**, *9* (2), 91–102. https://doi.org/10.1007/s12551-016-0247-1

Prasad, P. N.; Ulrich, D. R. *Nonlinear optical and electroactive polymers*. Springer Science & Business Media, 2012.

Pretsch, E.; Clerc, T.; Seibl, J.; Simon, W. *Tables of spectral data for structure determination of organic compounds*. Springer Science & Business Media, 2013.

Ray, P. C. Size and shape dependent second order nonlinear optical properties of nanomaterials and their application in biological and chemical sensing. *Chem. Rev.* **2010**, *110* (9), 5332–5365. https://doi.org/10.1021/cr900335q

Saminathan, M.; Jayakumar, M. R.; Chandrasekaran, R.; Raja, R.; George, J.; Alagusundaram, P. Synthesis, spectral, crystal structure, drug-likeness, in silico and in vitro biological screening of halogen [Cl, Br] substituted *N*-Phenylbenzo [*g*] indazole derivatives as antimicrobial agents. *J. Heterocycl. Chem.* **2021**, *58* (3), 841–863. https://doi.org/10.1002/jhet.4219

Sruthi, S. N.; Shyleshchandran, M. S.; Mathew, S. P.; Ramasamy, E. V. Contamination from organochlorine pesticides (OCPs) in agricultural soils of Kuttanad agroecosystem in India and related potential health risk. *Environ. Sci. Pollut. Res.* **2017**, *24* (1), 969–978. https://doi.org/10.1007/s11356-016-7834-3

Suresh, S.; Gunasekaran, S.; Srinivasan, S. Spectroscopic (FT-IR, FT-Raman, NMR and UV– Visible) and quantum chemical studies of molecular geometry, Frontier molecular orbital, NLONBO and thermodynamic properties of salicylic acid. *Spectrochim. Acta A Mol. Biomol. Spectrosc.* **2014**, *132*, 130–141. https://doi.org/10.1016/j.saa.2014.04.174

Tadesse, T. Quantum Mechanical Study on the Effect of Solvent in the Properties of Benzophenone. *J. Phys. Chem. Biophys.* **2017**, *7* (4) 1000259. https://doi.org/10.4172/2161-0398.1000259

Yang, W. H.; Wang, Z. Y.; Liu, H. L.; Yu, H. X. Exploring the binding features of polybrominated diphenyl ethers as estrogen receptor antagonists: docking studies. *SAR QSAR Environ. Res.* **2010**, *21* (3–4), 351–367. https://doi.org/10.1080/10629361003773971

Zhang, Y.-x.; Wang, Y.-h. Nonlinear optical properties of metal nanoparticles: a review. *RSC Adv.* **2017**, *7* (71), 45129–45144. https://doi.org/10.1039/C7RA07551K

Zhang, R.; Li, P.; Zhang, R.; Shi, X.; Li, Y.; Zhang, Q.; Wang, W. Computational study on the detoxifying mechanism of DDT metabolized by cytochrome P450 enzymes. *J. Hazard. Mater.* **2021**, *414*, 125457. https://doi.org/10.1016/j.jhazmat.2021.125457

Eclética Química Journal, vol. 47, n. 3, 2022, 39-52
ISSN: 1678-4618
DOI: 10.26850/1678-4618eqj.v47.3.2022.p39-52